Journal of Electron Spectroscopy and Related Phenomena 274 (2024) 147452

Contents lists available at ScienceDirect

Journal of Electron Spectroscopy and Related Phenomena

journal homepage: www.elsevier.com/locate/elspec

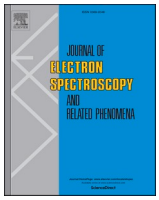

Mn 2p and O 1s X-ray absorption spectroscopy of manganese oxides

Haytham Eraky [a], James J. Dynes [b], Adam P. Hitchcock [a,*]

[a] Dept of Chemistry & Chemical Biology, McMaster University, Hamilton, ON L8S4M1, Canada
[b] Canadian Light Source, Saskatoon, SK S7N2V3, Canada

ARTICLE INFO

Keywords:
X-ray Absorption Spectroscopy
Manganese oxides
Scanning transmission X-ray microscopy, STXM
Total electron yield (TEY)
Zinc ion batteries

ABSTRACT

Manganese oxides (MnOx) are used as electrode materials in many different energy storage applications such as batteries and supercapacitors. X-ray spectromicroscopy, using near edge X-ray absorption spectra (NEXAFS) for chemical speciation, is a powerful tool to study reduction and oxidation processes in such systems. High quality reference spectra are required for both qualitative identification and quantitative mapping of MnOx species. Here we present accurate, quantitative Mn 2p and O 1s NEXAFS spectra of MnO, $MnSO_4$, Mn_3O_4, Mn_2O_3, α-MnO_2, β-MnO_2, and $KMnO_4$, measured using both transmission and total electron yield X-ray absorption techniques. An example of the use of these reference spectra in a study of Zn/MnO_2 batteries is given.

1. Introduction

Recently, manganese oxides (MnOx) have been used widely as electrode materials in different energy storage systems such as supercapacitors [1], batteries [2] and fuel cells [3]. MnOx have attracted this great interest owing to their high theoretical capacitance, rich redox reactions and varied crystal structures. In addition, manganese is an environmentally friendly and earth-abundant element [4,5]. MnOx species are the most common positive electrode material used in supercapacitors [6,7] and in non-aqueous primary or secondary lithium-ion batteries (LIBs) such as those used in electric vehicles [8,9]. Manganese metal is a d-block element with five unpaired 3d electrons in the neutral state ([Ar]$3d^5s^2$). It has a wide range of stable oxidation states: Mn(II), Mn(III), Mn(IV), Mn(VII), as well as a mixed valence Mn (II/II) state [5,10,11]. Manganese can establish different bonds with oxygen which create a wide range of stoichiometric oxides, hydroxides, and oxyhydroxides (collectively referred to as "manganese oxides" (MnOx)) [5]. Mn-O bonds are generally ionic but with some covalent character. The covalent character increases with increasing oxidation state. Lower Mn oxidation states (eg. Mn(II)) are more ionic, while higher oxidation states (Mn(VII)) are more covalent [12].

In order to optimize the performance of energy conversion devices based on MnOx chemistry, characterization techniques with quantitative mapping capabilities (i.e. spectromicroscopies) are needed to provide information about the spatial distributions of different Mn species (oxidation state, and possibly phase) and how the species and their spatial distributions might change during electrochemical processes. Such studies can provide mechanistic insights into charge storage and conversion mechanisms in different energy storage applications [4–9, 13], that can provide leads to developing enhanced energy materials. Scanning transmission X-ray microscopy (STXM) is a powerful synchrotron-based, soft X-ray spectromicroscopic technique [14–16] that uses near edge X-ray absorption spectra (NEXAFS) [17] to identify chemical species and provide quantitative, chemically selective imaging at sub-30 nm spatial resolution.

To fully exploit the capabilities of STXM, it is important to have reliable, accurately calibrated, quantitative NEXAFS spectra of each species of interest. The Mn 2p [10–13,15,18–28] and O 1s[11,12,22,23, 29] NEXAFS spectra of the common MnOx species have been published multiple times, and there is general agreement on spectral **shapes**. However, there are significant discrepancies in the **energy positions** of the characteristic O 1s and Mn 2p spectral features. For example, all of the features in the Mn 2p spectra of the MnO_x species reported by Toner et al. [19] are 1.0 – 1.8 eV higher than the corresponding results reported by Gilbert et al. [12]. Since these discrepancies are much larger than peak shifts typically used in determination of oxidation states, it is important to resolve these differences. Thus, we have carried out systematic measurements of the Mn 2p and O 1s NEXAFS spectra of the common manganese oxides using both transmission and total electron yield (TEY) detection. In this work, we report accurately calibrated and quantitative Mn 2p and O 1s NEXAFS spectra of MnO, $MnSO_4$, Mn_3O_4, Mn_2O_3, α-MnO_2, β-MnO_2 and $KMnO_4$.

Our main focus in this work is to establish definitive energies of spectral features in the Mn 2p and O 1s NEXAFS spectra of the common

* Corresponding author.
E-mail address: aph@mcmaster.ca (A.P. Hitchcock).

https://doi.org/10.1016/j.elspec.2024.147452
Received 12 December 2023; Received in revised form 25 May 2024; Accepted 28 May 2024
Available online 8 June 2024

MnO_x species. Assignments of the Mn 2p and O 1s spectral features have been discussed in detail elsewhere [12,20,23,24,27,28,30]. Thus we refer the reader to those references for detailed spectral assignments. The underlying interactions giving rise to the spectral features are well known. For completeness, a broad overview of their origin has been included in supplemental information section, **SI.1**.

2. Experimental procedures

2.1. Materials

Analytical grade manganese oxides were obtained commercially and used without purification: MnO (99.99 %, Alfa Aesar), $MnSO_4{\cdot}H_2O$ (≥99 %, Sigma-Aldrich), Mn_2O_3 (99.9 %, Sigma-Aldrich), Mn_3O_4 (synthesized chemically [31]), α-MnO_2 (≥99.99 %, Alfa Aesar), β-MnO_2 (≥90 %, Sigma-Aldrich) and $KMnO_4$ (99 %, Sigma-Aldrich). All chemicals were used as received, without further purification.

2.2. Powder X-ray diffraction

X-ray diffraction (XRD) analysis of each compound was performed (Bruker D8, Cu-Kα radiation). The XRD patterns were recorded from 10° to 80° at a scan rate of 1 degree per min. **Figure S.1** in **SI.2** presents the X-ray diffraction patterns of the MnO, $MnSO_4$, Mn_3O_4, Mn_2O_3, α-MnO_2 and $KMnO_4$ samples studied. Comparison of the observed diffraction patterns with those in the Joint Committee on Powder Diffraction Standards (JCPDS) data base indicates pure phases for all measured species: manganosite, MnO (JCPDS PDF 04–008–0277); szmikite, $MnSO_4{\cdot}(H_2O)$ (JCPDS PDF 04–008–9679); bixbyite, Mn_2O_3 (PDF 00–041–1442); hausmannite, Mn_3O_4 (JCPDS PDF 001–1127); pyrolusite, α-MnO_2 (JCPDS PDF 00–044–0141); and potassium permanganate, $KMnO_4$ (JCPDS PDF 04–008–2764).

2.3. X-ray absorption spectroscopy by STXM

Mn 2p and O 1 s X-ray absorption spectra were measured in transmission mode using the ambient STXM at the spectromicroscopy (SM) beamline, 10ID1 [32] at the Canadian Light Source (CLS, Saskatoon, Canada). STXM samples were prepared by (i) grinding the sample to a fine powder, (ii) depositing the powder on a silicon nitride (Si_3N_4) window (0.5 mm×0.5 mm in a 5 mm×5 mm silicon frame, Norcada, Inc.) attached to a trapezoidal STXM sample plate using double sided tape, and (iii) tapping the plate on a hard surface to detach the larger, weakly adhering particles. STXM measurements were performed after pumping the chamber to ~0.1 mbar, then back filling with He to a pressure of ~100 mbar. In STXM the monochromated X-ray beam is focused by a Fresnel zone plate (ZP) to a 40 nm spot. At each photon energy, a two-dimensional image is recorded by raster scanning the sample through the focused X-ray beam, while recording the intensity of transmitted X-rays with a phosphor/ photomultiplier tube detector [33]. Spectroscopic data was collected by measuring a sequence of images (collectively, called a stack [34]) at X-ray energies from ~10 eV below to ~40 eV above the onset of Mn 2p and O 1 s absorption. Images were recorded after measuring each Mn 2p and O 1s stack to investigate the possibility of radiation damage. Radiation damage was not detected in any of the measured samples, as determined by the similarity of the pre- and post-stack imaging.

2.4. X-ray absorption spectroscopy by total electron yield (TEY)

Mn 2p and O 1s X-ray spectra were also measured in TEY mode at the spherical grating monochromator (SGM) beamline 11ID-1 [35] at the CLS. The samples for total electron yield (TEY) spectroscopy were prepared by grinding the material and pressing the resulting powder into indium foil which was then mounted on a SGM sample support. The TEY measurements were conducted under vacuum at room temperature by collecting the total current from the sample as a function of photon energy. The spectra were measured in both fast scan and step scan mode with the X-ray beam focused to a 25 μm diameter spot size. In the fast scan mode, the photon energy is scanned continuously while taking time stamped measurements of the energy and current as fast as possible (ms sampling). After the fast scan acquisition, the data is interpolated onto an evenly spaced energy grid. In both fast scan and step scan modes, TEY spectra were measured at 10 different positions of the sample, then averaged. The fast scan mode and multiple, different-area measurements are used to minimize the X-ray dose. We did not observe any changes in the spectra that could indicate radiation damage, even in the higher dose step scan mode.

The incident beam intensity (Io) was recorded as the current from a gold mesh which was mounted before the final Kirkpatrick-Baez focussing mirrors. While the Io was typically featureless at the Mn 2p edge, the O 1s signal was structured from oxygen in the silicon oxy-nitride windows, from O_2 bled into the M1 and monochromator tanks to remove carbon contamination, and from oxide contamination of optical surfaces, as shown in **SI.3, Fig. S.2**. The O 1s spectral structure in the Io signal was stable so that it did not affect the spectral shape. The total fluorescence yield (TFY) and partial fluorescence yield (PFY) spectra were also measured simultaneously with the TEY. However, we found those spectra differed significantly from the STXM and TEY spectra, due to absorption saturation. Even using the inverse partial fluorescence yield (IPFY) approach [36], which generally reduces spectral distortion from absorption saturation, did not give correct results. **SI.4, Fig. S.3** compares the α-MnO_2 absorption spectrum measured in TEY, TFY and PFY modes. The Mn $2p_{3/2}$ characteristic features of α-MnO_2 (sharp peak at 640.5 eV and broad peak at 642.9 eV) are clearly observed in all three spectra but the TEY spectrum is the only one with the correct spectral shape, since the TFY and PFY spectra are significantly distorted by absorption saturation.

2.5. Comparison of STXM-NEXAFS and TEY-XAS

NEXAFS spectra recorded without spatial resolution gives similar spectroscopy as STXM, often with better statistical precision. TEY is a surface sensitive technique with a sampling depth of a few nanometers [37], whereas STXM is bulk-sensitive in that the NEXAFS spectrum is averaged over the full thickness of the sample, which is typically 10 – 200 nm thick. For samples thicker than ~100 nm absorption saturation can distort the O 1s and Mn 2p NEXAFS spectra when measured in transmission. An example of that is presented in **SI.5.** For TEY-XAS there are concerns that the spectrum may not be of the correct species since surface oxidation of low Mn oxidation state species can occur during sample preparation or storage, particularly for Mn metal [38] and Mn^{2+} compounds [39]. In contrast to STXM, where measurements are typically performed on individual particles over an area of several μm^2, the TEY measurements performed in this work are ensemble-averaged X-ray absorption spectra (XAS) measured from areas larger than 0.06 mm^2 of sample.

2.6. Data analysis

The STXM and TEY data were analyzed using aXis2000 software [40]. For STXM, the transmitted X-ray flux *(I)* was converted to optical density (OD) using the Beer–Lambert Law: $OD = -ln\ (I/Io)$, where the incident beam *(Io)* is recorded from a region devoid of the sample but with the support (typically silicon nitride, Si_3N_x) present. The TEY spectra are the ratio of the sample current to the Io from the upstream gold mesh. In order to obtain Mn 2p and O 1s reference spectra with an absolute OD1 scale (1 nm spectral response of the material at standard density [41]), the OD spectra of the measured MnOx samples were scaled to match the pre-edge and post-edge signals to the X-ray absorption elemental response predicted for 1 nm thickness of the compound formula using the elemental X-ray absorption coefficients [42]

and the standard densities of each compound: MnO (5.37 g/cm^{-3}), $MnSO_4$ (3.25 g/cm^{-3}), Mn_3O_4 (4.85 g/cm^{-3}), Mn_2O_3 (4.50 g/cm^{-3}), α-MnO_2 (5.08 g/cm^{-3}), β-MnO_2 (5.18 g/cm^{-3}) and $KMnO_4$ (2.70 g/cm^{-3}) [43]. An example of this conversion process is given in supplemental information, **section SI.6.** There are many review articles discussing STXM data analysis [14,40,41,44,45]. Readers are referred to these articles for further details on how OD1 reference spectra are generated and used to fit image sequences.

2.7. Spectral energy calibration

The energy scales at the Mn 2p edge of the SM and SGM beamlines were calibrated using the F 1s → $a_{1\ g}$ transition of SF_6 gas at 688.27 eV [46] and at the O 1s edge using either the O 1s → Π* transition of O_2 gas at 530.8 eV [46,47] or the O 1s → 3stransition of CO_2 gas at 538.9 eV [48]. At the SGM beamline, the gas phase spectra were recorded in transmission by measuring the photodiode signal in the SGM tank with and without SF_6 or CO_2 gas. This calibration was performed in the same run as the TEY measurements since significant (>1 eV) differences in peak positions were noted in different runs. The energy scale of the SM beam line was similarly calibrated using gas phase spectra of SF_6 and CO_2. Supplemental information, **section SI.7** presents examples of the energy scale calibration with these gases.

During measurements of several Cu 2p and Ni 2p compounds at the CLS SGM beamline, differences in the $2p_{3/2} - 2p_{1/2}$ spin orbit splitting of up to 0.5 eV were noted relative to the corresponding spin-orbit splitting measured by STXM at the CLS SM beamline. We attribute the discrepancies to non-linearity of either (or possibly both) of the SM or SGM beamline energy scales. For this work, the Mn $2p_{3/2} - 2p_{1/2}$ spin-orbit splitting in the same compound measured with the SM and SGM beamlines were found to differ by ~0.2 eV. Thus, while flagging this observation as an issue at higher energy edges where the spin-orbit splitting is larger, we are satisfied that a possible non-linearity over the ~15 eV of the Mn $2p_{3/2} - 2p_{1/2}$ spin-orbit splitting is within other uncertainties of our measurements. As shown in the next section, the Mn 2p spectra measured by STXM and TEY are very similar in both spectral shape and peak positions.

Perhaps of greater concern is a possible error in the Mn 2p energies due to a systematic non-linearity in the energy scales of the two beamlines used in this work. This issue is discussed in detail in section **SI.8**. We conclude from those considerations that any systematic error is at most 0.2 eV.

To evaluate the energy scale stability of the CLS-SM beamline over long periods of time, the positions of the characteristic Mn 2p features of the MnO_x species were tracked over the course of a 5-day run. These results are presented in **SI.9**, **Fig. S.9**. The deviation over the 5 days was less than 0.2 eV. Additionally, Mn 2p and O 1s signals from MnO were observed in the Io spectra which arose from contamination of the STXM zone plate. These signals were used to further validate the stability of the Mn 2p and O 1s energy scales over the course of the 5-day run, again indicating the energy scale was stable to within 0.2 eV.

3. Results

3.1. Mn 2p spectra of manganese oxides

Mn 2p spectra of different Mn oxides typically consist of one major peak accompanied by several minor, but often sharp, peaks in each of the Mn $2p_{3/2}$ and $2p_{1/2}$ spin-orbit split bands. The overall spectral shape and the energies of the sharp peaks can be used to identify and differentiate each of the Mn oxides species.

Fig. 1 presents the Mn 2p OD1 spectra of MnO, $MnSO_4$, Mn_3O_4, Mn_2O_3, α-MnO_2 and $KMnO_4$ measured by both STXM (thick solid line) and TEY-XAS (thin solid line). Note that $KMnO_4$ was only measured by TEY-XAS and MnO was only measured by STXM. The energies and proposed assignments of the main spectral features are summarized in

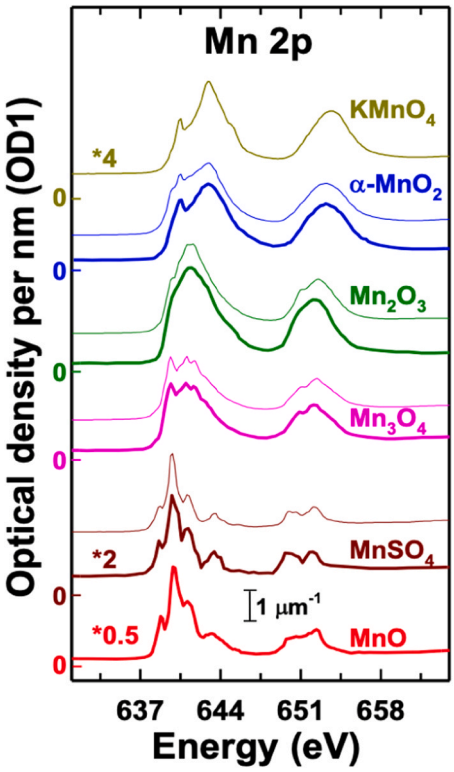

Fig. 1. Mn 2p spectra of MnO, $MnSO_4$, Mn_3O_4, Mn_2O_3, α-MnO_2 and $KMnO_4$ measured by STXM (thick solid line) compared to those measured by TEY (thin solid line). The STXM-derived spectra are presented on quantitative OD1 intensity scales, with offsets for clarity. The intensities of the TEY spectra have been scaled and offset to best match the corresponding STXM spectra.

Table 1 along with comparison to literature results. The Mn 2p spectra of each species are discussed individually in the following sections.

3.1.1. MnO and $MnSO_4$

The high-spin ground state of Mn^{2+} (MnO and $MnSO_4$, in this case) has a total of five unpaired electrons in the $t_{2\ g}$ and e_g orbitals ($t_{2\ g}^3$, e_g^2) [10,49]. The dominant feature of the Mn 2p spectrum of $MnSO_4$ is a very intense peak at 639.8 eV which is accompanied by lower intensity peaks at 638.7 eV, 641.1 eV and 643.4 eV in the $2p_{3/2}$ band, and two broad peaks at 650.0 eV and 652.0 eV in the $2p_{1/2}$ band. The overall shape of the Mn 2p spectrum of $MnSO_4$ is close to those reported in the literature [18,26]. However, there is considerable variation in the intensity of the finer features**.** The main spectral features match those reported by Risch et al. [26], but with 1.2 eV energy scale deviation **(**Table 1**)**.

The Mn 2p spectrum of MnO is very similar to that of $MnSO_4$. It exhibits a very intense L_3 peak at 639.7 eV and lower intensity peaks at 638.6 eV, 640.9 eV and 642.9 eV. The $2p_{1/2}$ band exhibits two broad peaks at 650.4 and 652.1 eV, with minor peaks at 649.5 and 651.5 eV. Although there is some variation in the intensity of finer features, the overall "triplet-like" shape of the MnO spectrum is in agreement with the spectra reported in the literature [10,12,19,26]. It is noteworthy that getting high quality Mn 2p spectra of MnO is very challenging when using transmission detection. The intensity of the main $2p_{3/2}$ peak at 639.7 eV is dramatically affected by absorption saturation even for samples thinner than 30 nm. In order to obtain the spectrum of MnO reported in this work, an embedded and microtomed section with an average thickness of 80 nm was prepared and measured. The Mn 2p spectrum reported here was extracted from a very small particle with ~10 nm thickness. Adjacent particles which were more than 30 nm thick were distorted by absorption saturation (see **SI.5, Fig. S.4**). Interestingly the Mn 2p spectrum of MnO reported by Risch et al. [26]

Table 1
Oxidation states and positions of major peaks in the Mn $2p_{3/2}$ spectra of manganese oxides, in comparison to literature results.

Sample	Mn Oxidation state	Major $2p_{3/2}$ peak position (eV)								
		This work	Ref [12]	ΔE(eV)[(a)]	Ref [19]	ΔE(eV)[(a)]	Ref [26]	ΔE (eV)[(a)]	Ref [10]	ΔE (eV)[(a)]
		638.6	639.1	0.5	637.5	1.1	–	–	639.3	0.7
MnO	+2	639.7	640.3	0.6	638.5	1.2	–	–	640.3	0.6
		640.9	641.4	0.5	639.9	1.0	–	–	641.7	0.8
		638.7	–	–	–	–	640.0	1.3	–	–
$MnSO_4$	+2	639.8	–	–	–	–	641.1	1.3	–	–
		641.1	–	–	–	–	642.4	1.3	–	–
		639.6	639.5	0.1	–	–	–	–	640.2	0.6
Mn_3O_4	+2/+3	641.0	640.9	0.1	–	–	–	–	641.8	0.8
		641.7	641.6	0.1	–	–	–	–	642.3	0.6
Mn_2O_3	+3	641.4	641.5	0.1	640.1	1.3	642.4	1.0	641.8	0.4
α-MnO_2	+4	640.5	640.5	<0.1	639.3	1.2	–	–	–	–
		642.9	643.0	0.1	641.7	1.2	–	–	–	–
β-MnO_2	+4	640.5	640.5	<0.1	639.3	1.2	–	–	641.0	0.5
		643.5	643.0	0.5	641.7	1.8	–	–	643.8	0.3
$KMnO_4$	+7	640.5	640.4	0.1	–	–	–	–	–	–
		642.9	642.8	0.1	–	–	–	–	–	–

(a) ΔE is the peak energy measured in this work minus that given in the cited reference.

was measured in TEY mode from the surface of a nominally pure metallic Mn sample. This indicates both the ease with which low oxidation states of Mn can oxidize in contact with air, and also the surface sensitivity of TEY detection. Fig. 2 compares the Mn $2p_{3/2}$ spectra of MnO and $MnSO_4$. Both spectra exhibit similar $2p_{3/2}$ and $2p_{1/2}$ (see Fig. 1) spectral features. Nonetheless, the minor $2p_{3/2}$ peaks and the main $2p_{1/2}$ peaks of MnO and $MnSO_4$ have somewhat different intensities and peak positions (deviation of 0.1–0.5 eV), indicating that high quality Mn $2p_{3/2}$ spectra can differentiate Mn(II) sulphate and Mn (II) oxide species. In addition, we note there is a large difference between the Mn 2p feature energies we observe for $MnSO_4$ and those reported by Risch et al. [26]. We note that the manganese sulphate studied in this work is the tetrahydrate, whereas Risch et al. [26] measured the monohydrate. Thus, the differences could be due to the specific hydrate studied. Hydrates are susceptible to change when they are subjected to vacuum conditions, which may be an issue in this case. Not unexpectedly, there is an even larger difference in the O 1 s spectra of MnO and $MnSO_4$, as shown and discussed below (Section 3.2).

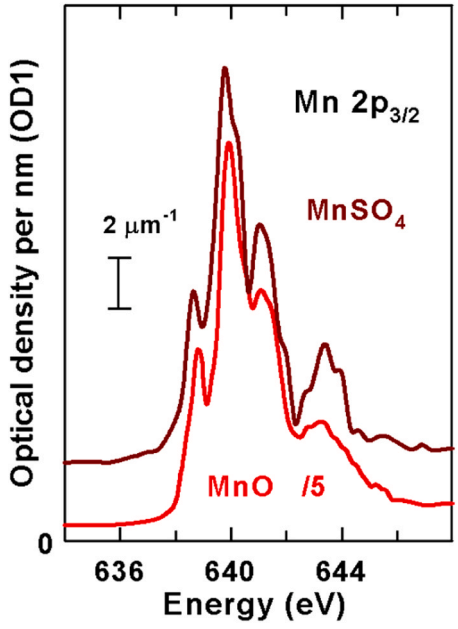

Fig. 2. Expansion of Mn L_3 spectra of MnO and $MnSO_4$ measured by STXM. The zero-signal level is valid for both spectra (i.e. there is no offset applied to the $MnSO_4$ spectrum. The OD1 intensity is given by the combination of the scale bar ($2\mu m^{-1}$) and the gain factor (/5) for MnO.

3.1.2. Mn_3O_4

Mn_3O_4 (Hausmannite) has a complex crystal structure with a 1:2 mixture of Mn^{2+} and Mn^{3+} cations [10] and a formal average oxidation state of +2.67. It can be represented by the formula, $Mn^{2+}(Mn^{3+})_2O_4$ [5]. The Mn 2p spectrum of Mn_3O_4 (Fig. 1) is in agreement with the literature spectra [11,12]. It consists of an initial sharp $2p_{3/2}$ peak at 639.6 eV, characteristic of Mn^{2+}, followed by two small peaks at 641.0 eV and 641.7 eV which can be related to the Mn^{3+} site. The STXM and TEY spectra have the same $2p_{3/2}$ and $2p_{1/2}$ energy scale and characteristic features, with < 0.1 eV deviation in the position of the two $2p_{3/2}$ lower intensity peaks. The first $2p_{3/2}$ peak at 639.6 eV is used to calibrate and compare Mn 2p spectra with reported reference spectra [11,12] (see Table 1). The Mn^{2+} and Mn^{3+} ions in Mn_3O_4 occupy tetrahedral and octahedral sites, respectively. The Mn^{3+} octahedral environment is affected by structural deformation (Jahn-Teller distortion) so that the Hausmannite crystal is distorted to a spinel tetragonal structure [10,50].

3.1.3. Mn_2O_3

The Mn 2p spectra of Mn_2O_3 measured by STXM and TEY measurements consists of a broad peak at 641.4 eV with two shoulder peaks at 639.8 eV and 642.8 eV. Unlike the other manganese oxides, there is no clearly resolved multiplet splitting at the $2p_{3/2}$ edge. Mn_2O_3 has a d^4 configuration with a high-spin ground state ($t_{2g}^3 e_g^1$) [10,12]. Manganese (III) ions are octahedrally complexed but are subject to strong Jahn-Teller distortion which results from the odd number of electrons in the triply degenerate t_{2g} orbital [10]. The Jahn-Teller distortion causes elongation of the two trans Mn-O bonds which results in a reduction of symmetry from octahedral to tetragonal [10,12,23].

3.1.4. α-MnO_2 and β-MnO_2

The Mn 2p spectra of α-MnO_2 (hollandite) and β-MnO_2 (pyrolusite) are compared in Fig. 3**A**. The spectrum of α-MnO_2 exhibits a sharp peak at 640.5 eV and broad peaks at 642.9 eV and 653.2 eV. In addition, there is a minor $2p_{3/2}$ shoulder peak at 639.5 eV, which was also observed in earlier studies [20,25]. While the Mn 2p spectrum of β-MnO_2 is similar to that of α-MnO_2, the broad $2p_{3/2}$ peak occurs at 643.5 eV, shifted +0.6 eV shift compared to α-MnO_2 (Fig. 3**B**). Octahedrally coordinated MnO_2 has a $t_{2g}^3 e_g^0$ ground state configuration [11, 12] where the lower energy t_{2g} orbital and higher energy e_g orbital are generated from the crystal field splitting of the Mn 3d orbital [20]. The peaks at 640.5 eV and 642.9 eV (α-MnO_2) / 643.5 eV (β-MnO_2) correspond to Mn 2p excitations to the t_{2g} and e_g levels, respectively. The

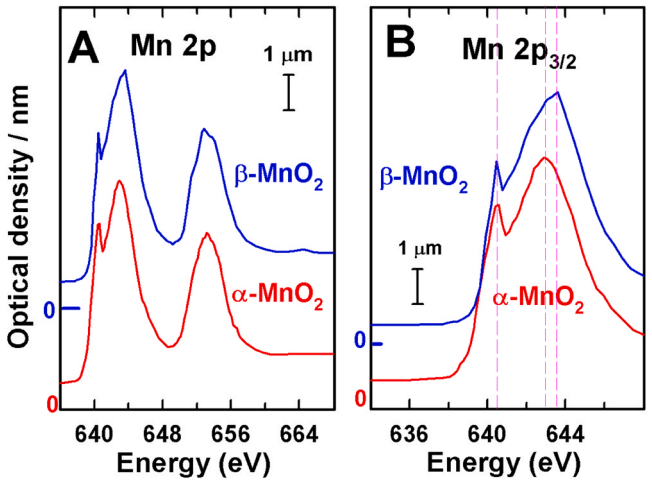

Fig. 3. Comparison of Mn 2p spectra of α-MnO_2 (hollandite) and β-MnO_2 (pyrolusite) **(A)** full range Mn 2p spectra of α-MnO_2 and β-MnO_2. **(B)** Expansion of Mn $2p_{3/2}$ spectra of α-MnO_2 and β-MnO_2 showing the shift in the position of the Mn $2p_{3/2} \rightarrow e_g$ peak.

positions of the main peaks in β-MnO_2 agree with those for β-MnO_2 reported by Gilbert et al. [12] within experimental uncertainty. However, they are 1.2 eV higher in energy than those reported for δ-MnO_2 (birnessite) by Toner et al. [19] (see **SI.10**, **Fig S.10** and Table 1).

3.1.5. $KMnO_4$

In the MnO^{4-} permanganate ion, the Mn is tetrahedrally coordinated in the +7 oxidation state with a ground state electronic configuration of $[Ar]3d^0 4s^0$ [51]. The large empty 3d density should lead to very intense Mn 2p → 3d transitions. In perfect tetrahedral symmetry, the crystal-field splitting of the metal d orbitals should be reversed compared to the octahedral t_2-e splitting. Therefore, in MnO^{4-}, the empty e orbital is the lowest unoccupied state, while the t_2 orbital is located at a higher energy. The Mn 2p spectrum of $KMnO_4$ shows peaks at 640.5 eV and 642.9 eV which are assignable to 2p excitations into the empty e and t_2 orbitals, respectively. There is also a broad $2p_{1/2} \rightarrow$ 3d peak at 653.7 eV. The measured Mn 2p spectra of $KMnO_4$ (TEY) and $KMnO_4$ reported by Gilbert et al. [12] have the same features, although the TEY spectrum shows a more pronounced shoulder at 644.9 eV. The Mn 2p spectrum of $KMnO_4$ is very close to that of α-MnO_2 in both spectral shape and peak positions. However, the intensity of the $2p_{3/2}$ broad peak corresponding to Mn 2p e_g orbital is relatively higher in $KMnO_4$ compared to that in MnO_2 spectra. The shapes and energy positions of the main Mn 2p peaks of MnO_2 and $KMnO_4$ are in agreement with those reported in the literature [12]. The calibrated $KMnO_4$ $2p_{3/2}$ peaks agree with those reported by Gilbert et al. [12] but the peak positions are 0.1 eV lower, while the $2p_{1/2}$ peaks differ by 0.5 eV. In addition, the $2p_{3/2}$ feature of $KMnO_4$ at 640.5 eV has a lower intensity than that reported by Gilbert et al. [12]. The intensity ratio between the lower and higher Mn $2p_{3/2}$ energy peaks of MnO_4^- (at 640.5 eV and 642.9 eV) is 0.65. This value is close to the value of 0.7 reported by Brydson et al. [52]. Nevertheless, the deviation in the intensity ratio, associated with a lower intensity of the low energy $2p_{3/2}$ characteristic peak, may be a result of photo-reduction during the sample measurement, which is expected when measuring highly reactive, high oxidation state metal oxides like $KMnO_4$.

3.2. O 1 s spectra of manganese oxides

Fig. 4 presents the O 1s spectra of MnO, $MnSO_4$, Mn_3O_4, Mn_2O_3, α-MnO_2 and $KMnO_4$ measured by both STXM (thick solid line) and TEY-XAS (thin solid line). The energies of the major features are compared to those reported in the literature in Table 2, along with tentative assignments. The O 1s spectra of the manganese oxides consist of two regions, (i) "pre-edge" peaks below 534 eV which arise from O 1s excitations to O 2p - Mn 3d hybridized orbitals which are characteristic of the oxidation state; and, (ii) broad peaks at higher energy (above 534 eV) which are O 1sexcitations to the O 2p conduction band, with

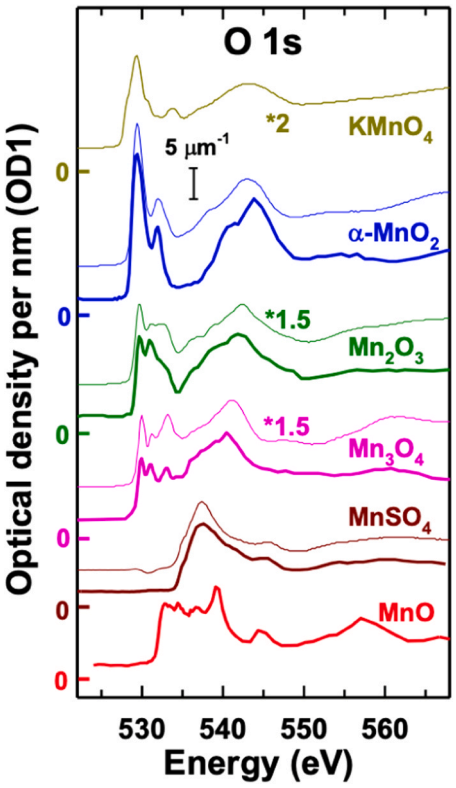

Fig. 4. O 1s spectra of MnO, $MnSO_4$, Mn_3O_4, Mn_2O_3, α-MnO_2 and $KMnO_4$ measured by STXM (thick solid line) compared to those measured by TEY (thin solid line). The STXM-derived spectra are presented on quantitative OD1 intensity scales, with offsets for clarity. The intensities of the TEY spectra have been scaled for best match to the STXM spectra.

Table 2
Major O 1s → 3d "pre-edge" peak position(s) of manganese oxides.

Sample	Mn Oxidation state	Major O 1 s → 3d pre-edge peaks position (eV)		
		This work	Ref [12]	ΔE (eV)[(a)]
MnO	+2	532.9	532.6	0.3
		534.4	533.9	0.5
		536.5	535.7	0.8
		539.1	539.0	0.1
		544.4	545.0	0.6
$MnSO_4$	+2	537.6	–	–
		545.2	–	–
Mn_3O_4	+2/+3	530.0	529.7	0.3
		531.1	531.5	0.4
		533.0	534.2	1.2
Mn_2O_3	+3	529.7	529.3	0.4
		530.9	530.7	0.2
		533.2	532.6	0.4
α-MnO_2	+4	529.4	528.9	0.5
		531.9	531.5	0.4
β-MnO_2	+4	529.4	528.9	0.5
		531.9	531.5	0.4
$KMnO_4$	+7	529.3	529.0	0.3
		530.7	531.2	0.5
		533.6	533.1	0.5

(a) ΔE is the peak energy measured in this work minus that given in the cited reference.

some interaction with Mn 4s and Mn 4p states [23,51].

3.3. MnO and $MnSO_4$

The STXM O 1s spectrum of MnO shows peaks at 532.9 eV, 534.4 eV, 536.5, 539.1, 544.4 eV, corresponding to O 1s → 3d excitations to t_{2g} (up), e_g (up), e_g (down) and 3d - 4sp features, respectively [12,27]. Aside from a systematic deviation of ~0.4 eV, the position and relative intensities of the spectral features of MnO are close to those reported by Gilbert et al. [12]. (see Table 2). The O 1s spectrum of $MnSO_4$ is significantly different from that of MnO in both spectral shape and peak positions. The STXM and TEY-XAS O 1s spectra of $MnSO_4$ are quite similar in both shape and peak positions, showing one major, broad peak at 537.6 eV and a minor, sharper peak at 541.5 eV.

Although the O 1s spectrum of MnO has been published elsewhere [11,12,23,27], the O 1s spectrum of $MnSO_4$ has not been reported in the literature, to the best of our knowledge. The Mn cation in MnO and $MnSO_4$ has a high spin $3d^5$ ground state with half-filled t_{2g} and e_g states. However, the different ligands and different Mn-ligand bond lengths [12,27] may lead to spectral differences. **Section S.11, Fig. S.11** compares the O 1s spectra of MnO and $MnSO_4$ with those of H_2SO_4 and the SO_3^- group in perfluorosulfonic acid. This comparison clearly indicates the effect of the SO_4^- or SO_3^- ligand on the O 1s spectral shape. MnO is a rock-salt octahedral coordination system [11,27]. The Mn^{2+} ion in $MnSO_4$ is in a slightly distorted octahedral environment [49] and the ligand field character of a sulfonate is significantly different from that of an oxide. The MnO O1s spectrum has a sharp O 1s → Mn 3d peak at 539 eV [11,12], and overlapping O 1s → –O 2p, Mn 4s, 4p features [27]. The measured $MnSO_4$ O 1s spectrum is also consistent with this observation; however, it has a stronger combination of the 3d and 4s, 4p parts of the spectrum which overlap as one peak.

3.3.1. Mn_3O_4 and Mn_2O_3

The O 1s STXM and TEY spectra of Mn_2O_3 and Mn_3O_4 exhibit similar O 1s → 3d features, with three peaks assigned to e_g-up, t_{2g}-down, and e_g-down [27] at 529.7 eV, 530.9 eV and 533.2 eV for Mn_2O_3 and 530.0 eV, 531.1 eV and 533.0 eV for Mn_3O_4 respectively. The spectra of each species match the spectral shape reported by Gilbert et al. [12], although there are energy scale deviations of 0.4 eV for Mn_2O_3 and 0.3 eV for Mn_3O_4 and a 1.2 eV deviation in the position of the third peak of the O 1s spectrum of Mn_3O_4 (see Table 2).

3.3.2. α-MnO_2 and β-MnO_2

The O 1s spectrum of α-MnO_2 and β-MnO_2 measured by STXM (see **Fig. S.12**) showed 2 sharp peaks in the O 1s → 3d "pre-edge" region at 529.4 eV and 531.9 eV and a broad peak at 543.8 eV. The first sharp peak at 529.4 eV is a combination of both spin-up e_g and the spin-down t_{2g} states, while the second sharp peak at 531.8 eV is related to spin-down e_g state [27]. The spectral shape and positions of peaks in the O 1s spectra of α-MnO_2 and β-MnO_2 are very similar. The TEY -XAS spectrum showed the same O 1s → 3d "pre-edge" peak positions and relative intensities as in the STXM spectrum. However, the broad peak observed at 542.9 eV in the STXM spectrum, corresponding to excitation to O 2p - Mn 4s, 4p hybridized states, was 1.0 eV lower in TEY-XAS. The spectral shapes are in agreement with that for MnO_2 reported by Gilbert et al. [12] but with an energy scale difference of 0.5 eV as shown in **SI.10**, **Fig. S.10** (see also Table 2).

3.3.3. KMnO

The O 1s spectrum of $KMnO_4$ has two O 1s → 3d pre-edge peaks at 529.3 eV and 533.6 eV, and a shoulder at 530.7 eV. These features have been assigned to O 1s promotions to $3de_g$-up, $3de_g$-down and $3dt_{2g}$-down, respectively [27]. There is also a broad peak at 543.2 eV corresponding to O 1s → O 2p - Mn 4s, 4p hybridized levels. The first sharp "pre-edge" peak at 529.3 eV was used to align the energy scale of our spectra with those reported in the literature [12,22].

3.3.4. Overall comparison of our spectra with literature spectra

The shapes of the Mn 2p and O 1s spectra of the MnOx reference compounds are in agreement with those reported earlier in the literature: Mn 2p [10–13,15,18–28] and O 1s [11,12,22,23,29]. The energy scales of the Mn 2p spectra reported here are very close to those reported by Gilbert et al. [12], with a maximum deviation of 0.2 eV. However, when compared to the δ-MnO_2 and Mn_2O_3 spectra reported by Toner et al. [18], there is a large deviation (on average, 1.3 eV, see Table 1). The degree of agreement with the literature O 1s spectra of MnO, Mn_3O_4, Mn_2O_3, α-MnO_2, β-MnO_2 and $KMnO_4$ [12] was somewhat worse than for the Mn 2p spectra (see Table 2). However, careful examination shows there is a systematic shift of +0.45 ± 0.12 eV relative to the values reported by Gilbert et al. [12]. We do note our O 1s spectral energies are derived from careful calibration to the sharp O 1s →3 s peak in CO_2(g) for which the energy is very well established [48]. In contrast, Gilbert et al. [12] used Mn_2O_3 as a standard and set the beamline energy scales accordingly. The observed systematic deviation in the O 1s energies would disappear if the assigned energy for the sharp low energy feature in the O 1s spectrum of Mn_2O_3 was reduced by 0.4 eV in the Gilbert et al. study.

3.4. Example of quantitative oxidation state mapping of an energy material

Detailed information about complex MnOx systems can be obtained by deriving quantitative component maps from Mn 2p and / or O 1s STXM image sequences using reference spectra on OD1 intensity scales [40,41]. The spatial distribution and quantitative thickness maps of each MnOx component can be obtained through least squares fitting using the efficient singular value decomposition (SVD) method [44]. Although stacks using the full Mn 2p spectrum give the best results, measuring only the Mn $2p_{3/2}$ (L_3) signal is usually enough to differentiate among Mn oxidation states. Simultaneous consideration of the O 1s and Mn 2p spectra provides additional information, as is well illustrated in section **SI.13** of the supplementary information. by a comparison of analysis of the Mn 2p stack alone, the O 1s edge alone, and analysis of the aligned and appended O 1s and Mn 2p stacks.

Fig. 5 presents quantitative chemical maps of the MnO, Mn_2O_3 and α-MnO_2 species in an α-MnO_2 cathode used in an experimental zinc-ion coin cell battery. These maps were obtained by fitting a Mn $2p_{3/2}$ STXM stack (70 energies, from 628 – 650 eV) to the quantitative OD1 reference spectra of MnO, Mn_2O_3 and α-MnO_2 compounds presented in this article. The intensity scales indicate the thickness of the indicated species in nm scale. Prior to this analysis the coin cell battery was subjected to 94 electrochemical charge (1.8 V) - discharge (1.2 V) cycles and left in the discharged state. After testing, the coin cell was taken apart and the cathode material was stripped off the separator, embedded in epoxy and microtomed to a thickness of 200 nm. Fig. 5**D** is a color-coded composite of the quantitative component maps of the three MnOx species.

After 94 charged cycles of the α-MnO_2 electrode, it was expected that α-MnO_2 will dominate all the sample as a result of oxidation processes. However, the results indicate that part of the α-MnO_2 was irreversibly reduced to MnO and Mn_2O_3 (Fig. 6**A**). In contrast, the Zn signals from the electrolyte ($ZnSO_4$) were observed in all MnOx regions, although with varying amounts (Fig. 6**B**). The quantitative chemical mapping showed that, despite a common understanding that this type of zinc-ion battery operates by shuttling Zn ions from the metallic Zn anode to channels in the α-MnO_2 in the cathode [53], these results indicate negligible co-location of Zn^{2+} and α-MnO_2 (Fig. 6**D**). If there was partial co-location, the α-MnO_2 region would be partly reduced to lower oxidation states. Instead, the lower oxidation state domains are completely separated from the α-MnO_2, indicating the existence of unreactive reduced Mn species (in particular MnO, see Fig. 6**C**). This is consistent with the low capacity of this battery after the 94-cycle testing.

Additionally, **section SI.13 (Fig. S.13)** compares the chemical mapping (in the form of color coded composite maps) of the 94-cycle

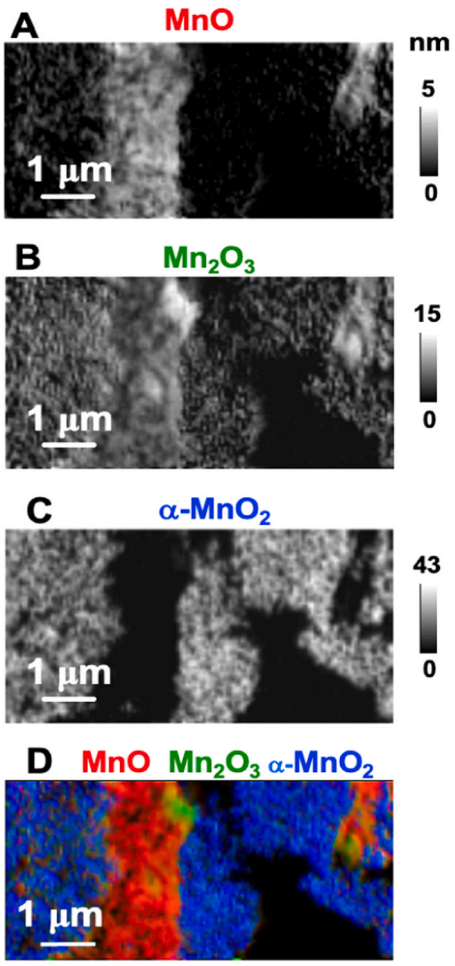

Fig. 5. Example of identification and quantitative mapping of MnOx species in a discharged, Zn/α-MnO_2 battery cathode after 94 charge / discharge cycles (left discharged). **(A)** MnO component map. The grey scale indicates thickness in nm. **(B)** Mn_2O_3 component map. **(C)** α-MnO_2 component map. (**D**) Rescaled color composite of MnO (red), Mn_2O_3 (green) and α-MnO_2 (blue) component maps.

discharge state MnO_2/ZIB sample obtained by fitting the Mn 2p stack (Fig. 5), the O 1s stack and the appended O 1s & Mn 2p stacks to the quantitative OD1 reference spectra of MnO, Mn_2O_3 and α-MnO_2. The first analysis using just the three MnO_x species in the fit revealed that there was an additional chemical component which only contributed to the O 1s stack. Further examination of the stack and isolation of the O 1s spectrum of the non-MnOx oxygen containing component showed this additional component was ZnO. Further details of this aspect of the results will be presented in a future publication. Comparisons and combined analysis of multiple edges, as explored in **SI.13** has significant advantages, such as revealing unexpected chemical species. Additionally, in thick samples where the Mn 2p spectra might be partially saturated, an O 1s edge study can provide additional support to the Mn 2p analysis.

4. Discussion

Our goal for this study was to measure high quality, accurately calibrated Mn 2p and O 1s spectra of common manganese oxides. This study was motivated by the significant (1–2 eV) deviation between Mn 2p feature energies reported by Gilbert et al. [12] and Toner et al. [19]. Our study has clearly shown that the energies reported by Toner et al. [19] are incorrect, whereas, aside from MnO, our Mn 2p energies agree with those reported by Gilbert et al. [12]. Interestingly the O 1s spectra

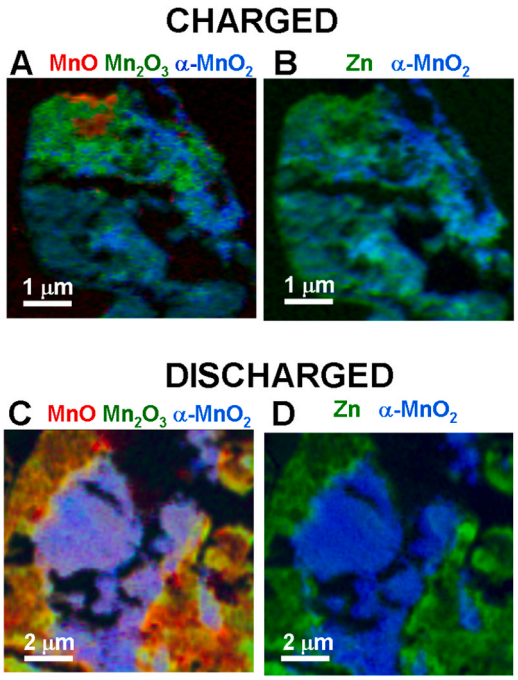

Fig. 6. Comparing Mn and Zn maps of 94-cycled, charged and discharged Zn/α-MnO_2 battery derived from Mn $2p_{3/2}$ and Zn 2p stacks. **(A)** Charged. Color coded composite of MnO (red), Mn_2O_3 (green), α-MnO_2 (blue) maps (rescaled) from a Mn $2p_{3/2}$ stack. **(B)** Charged. Color coded composite of Zn map (green, from Zn 2p stack) and α-MnO_2 map (blue, from Mn $2p_{3/2}$ stack) of the same region as (A) (rescaled). **(C)** Discharged. Color coded composite of MnO (red), Mn_2O_3 (green), α-MnO_2 (blue) maps (rescaled) from a Mn $2p_{3/2}$ stack. (**D**) Discharged Color coded composite of Zn map (green, from Zn 2p stack) and α-MnO_2 map (blue, from Mn $2p_{3/2}$ stack) of the same region as (C) (rescaled).

revealed a significant difference in energies relative to those reported by Gilbert et al. [12]. Given the use of the well-known, accurate spectra of O_2 or CO_2 (g) for energy scale calibration, we believe our O 1s energies are the more accurate.

STXM is a very powerful technique that provides spectroscopic characterization on a fine (sub 50 nm) spatial scale, which has significant advantages for quantitative mapping of chemical species in complex systems, such as polymer electrolyte membrane fuel cells (PEM-FC) [45]. Manganese-based oxides are efficient electrode materials for different energy storage systems, in particular for supercapacitors and batteries [7]. Identification of changing Mn oxidation states and their spatial distributions during different electrochemical processes can provide insights into charge transfer mechanisms [13]. Manganese oxides have various oxidation states (Mn^{2+} to Mn^{7+}) which, as shown in this study as well in the literature [10,12,19,26–30], have unique Mn 2p and O 1s spectral shapes and peaks positions which can be used to distinguish between different Mn oxidation states. Thus, the high-quality, accurately calibrated Mn 2p and O 1s pre-edge spectra provided in this research can be used to identify and map Mn oxidation states and intermediate components.

The Mn 2p and O 1s STXM and TEY-XAS spectra of the manganese oxides presented in Fig. 1 and Fig. 4 show there is a unique spectral shape for each Mn oxidation state. Nevertheless, there are some differences in the intensity of the finer features in spectra measured in TEY mode compared to those measured in transmission mode using STXM. These differences may be related to different energy resolution and/or surface oxidation/contamination. Mapping oxidation states can be performed using only the Mn $2p_{3/2} \rightarrow 3d$ features in the 630–650 eV region, which reduces acquisition time and radiation dose as compared to measuring full Mn 2p stacks. This can be particularly advantageous when performing *in-situ* STXM measurements [54–56], where speed of

acquisition is critical.

The differences in the Mn $2p_{3/2}$ spectra of α-MnO_2 and β-MnO_2 indicates sensitivity to crystal structure changes. The differences in the spectra of these polymorphs can be ascribed to a larger crystal field in β-MnO_2 resulting from greater delocalization of the excited 3d electron. The phase dependence of the Mn 2p spectrum of MnO_2 is similar to that observed in the Ti 2p XAS spectra of the anatase and rutile polymorphs of TiO_2 [57], where the main difference is the presence of a larger splitting and different peak intensities in the split Ti $2p \rightarrow e_g$ band in anatase, relative to that of rutile [57,58].

Detailed quantum chemistry calculations and comparison of the results to experimental Mn 2p and O 1 s spectra of the MnOx compounds have been reported in the literature [12]. Sherman et al. [59] reported molecular cluster calculations of the MnOx electronic structure. de Groot et al. [58] reported spectral calculations of 3d transition-metal compounds including Mn^{4+}, Mn^{3+}, and Mn^{2+} using atomic multiplet theory, which focused on the effect of a cubic crystal field on the shape of the $3d^N \rightarrow 2p^5\ 3d^{N+1}$ excitation spectra. A theoretical analysis of the O 1s spectra of $KMnO_4$ and MnO_2 was presented by Gilbert et al. [12] using spin dependent multiple scattering calculations. The peak separations predicted by that calculation are less than those in the experimental spectra.

Over the years, extensive effort has been devoted to quantitatively analyze mixed Mn oxidation states in complex systems using linear combination fitting (LCF) of X-ray absorption spectra at both the Mn 2p and Mn 1s edges. In 1996, Grush et. al. [30] measured the Mn 1s spectra of a Mn metallo-protein in both its reduced and super-oxidized states, and interpreted the measured spectra by LCF analysis using a combination of the spectra of $MnSO_4$ and $NBu_4[Mn_4O_2(O_2\text{-}CMe)_7(pic)_2]$ (pic = picolinate) as references [30]. Penner-Hahn et al. [60] presented the first use of LCF analysis of the Mn 1s spectrum of the manganese sites in the photosynthetic oxygen-evolving complex using combinations of the Mn 1s spectra of Mn(II), Mn(III) and Mn(IV). In this work, the ability to identify oxidation state content at individual pixels (as presented in the color coded composites of component maps, e.g. Fig. 5 and Fig. 6) allows a much more detailed approach to the quantitative analysis of mixture oxidation states systems. Section **S.14** provides an example of using quantitative chemical mapping by STXM to first, identify spatial regions that are mixtures of oxidation states, and then to quantify the composition by LCF fitting the spectrum of a selected set of pixels. In this example, the spectra of mixed oxidation state regions in the α-MnO_2/ZIB discharged electrode (the blue regions in **Fig. S.14B,** corresponding to yellow regions in Fig. 5**D**) are extracted and identified to be a mix of 3 nm MnO and 8 nm of Mn_2O_3.

As an example of the utility of Mn 2p spectroscopy in energy materials research, we have used the data presented here to perform quantitative analysis of Mn 2p and O 1s STXM results to track oxidation state changes after different electrode activation procedures of Mn_3O_4 supercapacitor electrodes [31,61]. In a second example, Wang et al. [13] used Mn 2p TEY-XAS to study Mn oxidation states in different, as-prepared, Mn-based supercapacitor electrodes and correlated these changes to achieved capacitance performance. The spectra presented in this work are the analytical basis for a number of research programs our group is performing. This includes applied projects such as ex situ studies of Mn_3O_4 based supercapacitors [31,61] and MnO_2 based Zn ion secondary batteries for large scale grid energy storage [53,56], as well as fundamental studies, such as *in situ* STXM studies of electrochemical modification of electrodeposited MnO_2 [56].

What are the long term implications/applications of these results ? One conceptual message is that *spectromicroscopy* is a better way to study heterogeneous materials than non-spatially resolved *spectroscopy*. The trend in new beamlines and end stations at synchrotron facilities is to develop imaging beamlines with spectroscopy capabilities, rather than non-spatially resolved, solely spectroscopy systems. As an illustration of this trend the reader might wish to consult a bibliography of soft X-ray spectromicroscopy articles (regularly updated and available at http://unicorn.mcmaster.ca/xrm-biblio/xrm_bib.html). This document lists and categorizes over 4000 articles using soft X-ray microscopy and spectromicroscopy published from 1969 to 2023. Over 2000 of these articles are based on STXM measurements. There are many, many different areas of application of soft X-ray spectromicroscopy. The number of both soft and hard X-ray STXMs continues to increase. For these systems to be most effective, accurate, quantitative reference spectra are required.

5. Summary

High quality calibrated, quantitative Mn 2p and O 1s NEXAFS spectra of six different manganese oxide compounds have been measured by STXM and TEY-XAS. An example of their use in the analysis of an electrochemically degraded zinc-ion battery cathode was given. STXM and X-ray absorption spectroscopy measurements of different energy storage systems can be analyzed with the spectra reported in this work to study changes in Mn valence during different electrochemical processes. All the Mn 2p and O 1s spectra are provided as supplemental information.

CRediT authorship contribution statement

Haytham Eraky: Writing – original draft, Formal analysis, Data curation. **James J. Dynes:** Formal analysis, Data curation. **Adam Hitchcock:** Writing – review & editing, Supervision, Software, Data curation, Conceptualization.

Declaration of Competing Interest

The authors declare the following financial interests/personal relationships which may be considered as potential competing interests: Adam Hitchcock (APH) reports financial support was provided by Natural Sciences and Engineering Research Council of Canada. APH recently (1 July 2023) stepped down as editor of JESRP. The other authors declare that they have no known competing financial interests or personal relationships that could have influenced the work reported in this paper.

Data availability

All reference spectra are available in the Supporting Information

Acknowledgements

We thank Chunyang Zhang for his assistance with making these measurements. Research was supported financially by the Natural Sciences and Engineering Research Council of Canada. X-ray diffraction was performed at the MAX facility at McMaster University. STXM and SGM measurements were performed at the CLS, which is supported by CFI, NSERC, CIHR, NRC and the University of Saskatchewan. We thank CLS staff scientists, Jian Wang (SM), Tom Regier and Zachary Arthur (SGM) for their support in carrying out these experiments. Some spectra were also measured at the STXM on beamline 11.0.2 at the Advanced Light Source, which is supported by the US Department of Energy under Contract No. DE-AC02–05CH11231. The Mn 2p and Zn 2p spectromicroscopy results for the 94-cycled discharged zinc ion battery sample were measured at the softiMAX beamline at MaxIV (Lund, Sweden), using beamtime allocated under proposal 20221375. Research conducted at MAX IV, a Swedish national user facility, is supported by the Swedish Research Council under contract 2018–07152, the Swedish Governmental Agency for Innovation Systems under contract 2018–04969, and Formas under contract 2019–02496. We thank the SoftiMAX staff scientists, Dr. Igor Beinik, Dr. Claudiu Bulbucan and Dr. Karina Thånell for their assistance in carrying out these experiments. We thank the reviewers of the paper for their comments and suggested

changes which significantly improved the manuscript.

Appendix A. Supporting information

Supplementary data associated with this article can be found in the online version at doi:10.1016/j.elspec.2024.147452.

References

[1] W. Wei, X. Cui, W. Chen, D.G. Ivey, Manganese oxide-based materials as electrochemical supercapacitor electrodes, Chem. Soc. Rreviews 40 (2011) 1697–1721.
[2] K. Rajagopalan, B. Ramasubramanian, S. Velusamy, S. Ramakrishna, A.M. Kannan, M. Kaliyannan, S. Kulandaivel, Examining the economic and energy aspects of manganese oxide in Li-Ion batteries, Mater. Circ. Econ. 4 (2022) 22.
[3] W. Elliott, R. Salemmilani, S. Mubeen, C.D. Meinhart, G.D. Stucky, M. Moskovits, Changes in the structure of electrodeposited manganese oxide water oxidation catalysts revealed by in-operando Raman spectroscopy, J. Catal. 371 (2019) 287–290.
[4] D. Guo, Z. Hu, Q. Li, L. Bian, Y. Song, X. Liu, Mixed-valence manganese oxide/reduced graphene oxide composites with enhanced pseudocapacitive performance, J. Mater. Sci. (2022) 1–13.
[5] S.K. Ghosh, Diversity in the family of manganese oxides at the nanoscale: from fundamentals to applications, ACS Omega 5 (2020) 25493–25504.
[6] J. Rodriguez-Romero, I. Ruiz de Larramendi, E. Goikolea, Nanostructured manganese dioxide for hybrid supercapacitor electrodes, Batteries 8 (2022) 263.
[7] N. Parveen, S.A. Ansari, M.Z. Ansari, M.O. Ansari, Manganese oxide as an effective electrode material for energy storage: a review, Environ. Chem. Lett. (2022) 1–27.
[8] F.N.U. Khan, M.G. Rasul, A. Sayem, N.K. Mandal, Design and optimization of lithium-ion battery as an efficient energy storage device for electric vehicles: a comprehensive review, J. Energy Storage 71 (2023) 108033.
[9] X. Zeng, M. Li, D. Abd El-Hady, W. Alshitari, A.S. Al-Bogami, J. Lu, K. Amine, Commercialization of lithium battery technologies for electric vehicles, Adv. Energy Mater. 9 (2019) 1900161.
[10] L. Garvie, A. Craven, High-resolution parallel electron energy-loss spectroscopy of Mn L2, 3-edges in inorganic manganese compounds, Phys. Chem. Miner. 21 (1994) 191–206.
[11] M. Risch, K.A. Stoerzinger, B. Han, T.Z. Regier, D. Peak, S.Y. Sayed, C. Wei, Z. Xu, Y. Shao-Horn, Redox processes of manganese oxide in catalyzing oxygen evolution and reduction: an in situ soft X-ray absorption spectroscopy study, J. Phys. Chem. C. 121 (2017) 17682–17692.
[12] B. Gilbert, B. Frazer, A. Belz, P. Conrad, K. Nealson, D. Haskel, J. Lang, G. Srajer, G. De Stasio, Multiple scattering calculations of bonding and X-ray absorption spectroscopy of manganese oxides, J. Phys. Chem. A 107 (2003) 2839–2847.
[13] Z. Wang, D. Yang, T.-K. Sham, Effect of oxidation state of manganese in manganese oxide thin films on their capacitance performances, Surf. Sci. 676 (2018) 71–76.
[14] A.P. Hitchcock, Soft X-ray spectromicroscopy and ptychography, J. Electron Spectrosc. Relat. Phenom. 200 (2015) 49–63.
[15] J.-D. Förster, I. Bykova, D.S. Macholdt, K.P. Jochum, M. Kappl, A.D. Kilcoyne, M. Müller, A. Sorowka, B. Weber, M. Weigand, X-ray microspectroscopy and ptychography on nanoscale structures in rock varnish, J. Phys. Chem. C. 125 (2021) 22684–22697.
[16] C. Jacobsen, X-ray Microscopy, Cambridge University Press, 2019.
[17] J. Stöhr, NEXAFS spectroscopy, in: Springer Series in Surface Science, Vol 25, Springer, Berlin, 1992.
[18] K. Pecher, D. McCubbery, E. Kneedler, J. Rothe, J. Bargar, G. Meigs, L. Cox, K. Nealson, B. Tonner, Quantitative charge state analysis of manganese biominerals in aqueous suspension using scanning transmission X-ray microscopy (STXM), Geochim. Et. Cosmochim. Acta 67 (2003) 1089–1098.
[19] B. Toner, S. Fakra, M. Villalobos, T. Warwick, G. Sposito, Spatially resolved characterization of biogenic manganese oxide production within a bacterial biofilm, Appl. Environ. Microbiol. 71 (2005) 1300–1310.
[20] F. Bourdelle, E. Lloret, C. Durand, L. Airaghi, Evaluation of scanning transmission X-ray microscopy at the Mn L2, 3-edges as a potential probe for manganese redox state in natural silicates, Phys. Chem. Miner. 48 (2021) 18.
[21] L. Galezowski, N. Recham, D. Larcher, J. Miot, F. Skouri-Panet, F. Guyot, Microbially induced mineralization of layered Mn oxides electroactive in Li batteries, Front. Microbiol. 11 (2020) 2031.
[22] M. Müller, M. Schellhorn, K. Mann, Laboratory-scale near-edge X-ray absorption fine structure spectroscopy with a laser-induced plasma source, J. Anal. At. Spectrom. 34 (2019) 1779–1785.
[23] R. Qiao, T. Chin, S.J. Harris, S. Yan, W. Yang, Spectroscopic fingerprints of valence and spin states in manganese oxides and fluorides, Curr. Appl. Phys. 13 (2013) 544–548.
[24] Y. Shi, J. Li, X. Zhang, K. Zhao, Z. Wang, Z. Wang, X. Peng, Regulating the pyrolysis process of cation intercalated MnO 2 nanomaterials for electrocatalytic urea oxidation performance, RSC Aadvances 12 (2022) 30605–30610.
[25] F.M. de Groot, E. de Smit, M.M. van Schooneveld, L.R. Aramburo, B. M. Weckhuysen, In-situ scanning transmission X-ray microscopy of catalytic solids and related nanomaterials, ChemPhysChem 11 (2010) 951–962.
[26] M. Risch, D.M. Morales, J. Villalobos, D. Antipin, What X-ray absorption spectroscopy can tell us about the active state of earth-abundant electrocatalysts for the oxygen evolution reaction, Angew. Chem. Int. Ed. 61 (2022) e202211949.
[27] L. Xi, C. Schwanke, J. Xiao, F.F. Abdi, I. Zaharieva, K.M. Lange, In situ L-edge XAS study of a manganese oxide water oxidation catalyst, 2017, J. Phys. Chem. C. 121 (2017) 12003–12009.
[28] M. Khan, E. Suljoti, A. Singh, S.A. Bonke, T. Brandenburg, K. Atak, R. Golnak, L. Spiccia, E.F. Aziz, Electronic structural insights into efficient MnOx catalysts, J. Mater. Chem. A *2* (2014) 18199–18203.
[29] F. Frati, M.O. Hunault, F.M. De Groot, Oxygen K-edge X-ray absorption spectra, Chem. Rev. 120 (2020) 4056–4110.
[30] M.M. Grush, J. Chen, T.L. Stemmler, S.J. George, C.Y. Ralston, R.T. Stibrany, A. Gelasco, G. Christou, S.M. Gorun, J.E. Penner-Hahn, S.P. Cramer, Manganese L-edge X-ray absorption spectroscopy of manganese catalase from Lactobacillus plantarum and mixed valence manganese complexes, J. Am. Chem. Soc. 118 (1996) 65–69.
[31] W. Yang, H. Eraky, C. Zhang, A.P. Hitchcock, I. Zhitomirsky, Scanning transmission X-ray microscopy studies of electrochemical activation and capacitive behavior of Mn_3O_4 supercapacitor electrodes, J. Mater. Chem. A 10 (2022) 18267–18277.
[32] K.V. Kaznatcheev, C. Karunakaran, U.D. Lanke, S.G. Urquhart, M. Obst, A. P. Hitchcock, Soft X-ray spectromicroscopy beamline at the CLS: commissioning results, Nucl. Instrum. Methods Phys. Res. Sect. A: Accel., Spectrometers, Detect. Assoc. Equip. 582 (2007) 96–99.
[33] A. Kilcoyne, T. Tyliszczak, W. Steele, S. Fakra, P. Hitchcock, K. Franck, E. Anderson, B. Harteneck, E. Rightor, G. Mitchell, Interferometer-controlled scanning transmission X-ray microscopes at the Advanced Light Source, J. Synchrotron Radiat. 10 (2003) 125–136.
[34] C. Jacobsen, S. Wirick, G. Flynn, C. Zimba, Soft X-ray spectroscopy from image sequences with sub-100 nm spatial resolution, J. Microsc. 197 (2000) 173–184.
[35] T. Regier, J. Krochak, T. Sham, Y. Hu, J. Thompson, R. Blyth, Performance and capabilities of the Canadian Dragon: the SGM beamline at the Canadian Light Source, Nucl. Instrum. Methods Phys. Res. Sect. A: Accel., Spectrometers, Detect. Assoc. Equip. 582 (2007) 93–95.
[36] A. Achkar, T. Regier, E. Monkman, K. Shen, D. Hawthorn, Determination of total x-ray absorption coefficient using non-resonant x-ray emission, Sci. Rep. 1 (2011) 182.
[37] M. Abbate, J. Goedkoop, F. De Groot, M. Grioni, J. Fuggle, S. Hofmann, H. Petersen, M. Sacchi, Probing depth of soft x-ray absorption spectroscopy measured in total-electron-yield mode, Surf. Interface Anal. 18 (1992) 65–69.
[38] J. Kawai, Y. Mizutani, T. Sugimura, M. Sai, T. Higuchi, Y. Harada, Y. Ishiwata, A. Fukushima, M. Fujisawa, M. Watanabe, High resolution soft X-ray absorption spectroscopy for the chemical state analysis of Mn, Spectrochim. Acta Part B: At. Spectrosc. 55 (2000) 1385–1395.
[39] Y. Gorlin, C.-J. Chung, J.D. Benck, D. Nordlund, L. Seitz, T.-C. Weng, D. Sokaras, B. M. Clemens, T.F. Jaramillo, Understanding interactions between manganese oxide and gold that lead to enhanced activity for electrocatalytic water oxidation, J. Am. Chem. Soc. 136 (2014) 4920–4926.
[40] A.P. Hitchcock, Analysis of X-ray images and spectra (aXis2000): A toolkit for the analysis of X-ray spectromicroscopy data, J. Electron Spectrosc. Relat. Phenom. 266 (2023) 147360.
[41] A.P. Hitchcock, Soft X-ray imaging and spectromicroscopy, Chapter 22 in Volume II of the Handbook on Nanoscopy, eds. Gustaaf Van Tendeloo, Dirk Van Dyck and Stephen J. Pennycook, Wiley, 2012.
[42] B.L. Henke, E.M. Gullikson, J.C. Davis, X-ray interactions: photoabsorption, scattering, transmission, and reflection at E= 50-30,000 eV, Z= 1-92, At. Data Nucl. Data Tables 54 (1993) 181–342.
[43] P. Patnaik, Handbook of Inorganic Chemicals, McGraw-Hill New York, 2003.
[44] I. Koprinarov, A. Hitchcock, C. McCrory, R. Childs, Quantitative mapping of structured polymeric systems using singular value decomposition analysis of soft X-ray images, The, J. Phys. Chem. B 106 (2002) 5358–5364.
[45] A.P. Hitchcock, PEM-FC analysis using soft X-ray spectromicroscopy: methods and applications, in: J. Stumper, J. Jankovic (Eds.), Chapter 5 in PEM Fuel Cells. Characterization and Modeling, de Gruyter, Berlin, Germany, 2023, pp. 137–169.
[46] R.N. Sodhi, C. Brion, Reference energies for inner shell electron energy-loss spectroscopy, J. Electron Spectrosc. Relat. Phenom. 34 (1984) 363–372.
[47] Y. Ma, C.T. Chen, G. Meigs, K. Randall, F. Sette, High-resolution *K*-shell photoabsorption measurements of simple molecules, Phys. Rev. A 44 (1991) 1848.
[48] K. Prince, L. Avaldi, M. Coreno, R. Camilloni, M. De Simone, Vibrational structure of core to Rydberg state excitations of carbon dioxide and dinitrogen oxide, J. Phys. B: ., Mol. Opt. Phys. 32 (1999) 2551–2567.
[49] P. Held, L. Bohatý, Manganese (II) sulfate tetrahydrate (ilesite), Acta Crystallogr. Sect. E: Struct. Rep. Online 58 (2002) i121–i123.
[50] J. Kaczmarek, E. Wolska, Cation and vacancy distribution in nonstoichiometric hausmanite, J. Solid State Chem. 103 (1993) 387–393.
[51] G. Greaves, K. Simkiss, M. Taylor, N. Binsted, The local environment of metal sites in intracellular granules investigated by using X-ray-absorption spectroscopy, Biochem. J. 221 (1984) 855–868.
[52] R. Brydson, L.A.J. Garvie, A.J. Craven, H. Sauer, F. Hofer, G. Cressey, $L_{2,3}$ edges of tetrahedrally coordinated d^0 transition-metal oxyanions XO_4^{n-}, J. Phys.: Condens. Matter 5 (1993) 9379–9392.
[53] Huanyan Liu, Jian-Gan Wang, Zongyuan You, Chunguang Wei, Feiyu Kang, Bingqing Wei, Rechargeable aqueous zinc-ion batteries: mechanism, design strategies and future perspectives, Mater. Today 42 (2021) 73–98.
[54] C. Zhang, H. Eraky, S. Tan, A.P. Hitchcock, D. Higgins, Simultaneously monitoring chemical and morphological changes in copper CO_2 reduction electrocatalysts by in-situ scanning transmission soft X-ray microscopy, ACS Nano 17 (2023) 21337–21348.

[55] C. Zhang, N. Mille, H. Eraky, S. Stanescu, S. Swaraj, R. Belkhou, D. Higgins, A. P. Hitchcock, Copper carbon dioxide reduction electrocatalysts studied by in situ soft X-ray spectro-ptychography, Cell Rep. Phys. Sci. 4 (2023) 101665.
[56] H. Eraky, Ex-situ and In-situ Soft X-Ray Spectro-Microscopy Studies of Manganese Oxide Electrodes for Energy Storage Applications (PhD Thesis), McMaster University, 2024.
[57] R. Ruus, A. Kikas, A. Saar, A. Ausmees, E. Nommiste, J. Aarik, A. Aidla, T. Uustare, I. Martinson, Ti 2p and O 1s X-ray absorption of TiO2 polymorphs, Solid State Commun. 104 (1997) 199–203.
[58] F.M. de Groot, J. Fuggle, B. Thole, G. Sawatzky, 2p x-ray absorption of 3d transition-metal compounds: an atomic multiplet description including the crystal field, Phys. Rev. B 42 (1990) 5459.
[59] D.M. Sherman, The electronic structures of manganese oxide minerals, Am. Mineral. 69 (1984) 788–799.
[60] J.E. Penner-Hahn, R.M. Fronko, V.L. Pecoraro, C.F. Yocum, S.D. Betts, N. R. Bowlby, Structural characterization of the manganese sites in the photosynthetic oxygen-evolving complex using x-ray absorption spectroscopy, J. Am. Chem. Soc. 112 (1990) 2549–2557.
[61] W. Yang, H. Eraky, C. Zhang, A.P. Hitchcock, I. Zhitomirsky, Scanning transmission X-ray microscopy of MnO_2 and Mn_3O_4 for supercapacitor cathodes influence of fabrication method and electrochemical activation on charge storage, Chem. Eng. J. 5 (2024) 149391.